CrossMark

Determination of Bond Strengths in Non-woven Fabrics: a Combined Experimental and Computational Approach

N. Chen[1] · M. N. Silberstein[1]

Abstract Interfiber bonds are important structural components in non-woven fabrics. Bond fracture greatly affects the strength and damage progression in a fiber network structure. Here, we present a novel combined experimental and computational approach to extract bond strengths in non-wovens. In this method, a small specimen is imaged and the obtained 3D geometry of the network is directly modeled in a finite element framework. Bond properties are determined by matching finite element simulation predicted mechanical response to the experimental data. This method is demonstrated by applying it to six specimens of a commercial polypropylene non-woven. A four parameter bi-linear interface law is used with normal stiffness k, shear stiffness βk, separation at the start of damage d_1, and separation at total loss of bond stiffness d_2. The determined normal strength (kd_1) and shear strength ($\beta k d_1$) are $(1.3 \pm 0.3) \times 10^2$ MPa and $(1.0 \pm 0.2) \times 10^2$ MPa, respectively. To show that the obtained bond parameters can be applied to a new specimen, a cross validation is conducted whereby parameters are fit from five specimens and then evaluated on the sixth. Additional validation of the obtained bond strength parameters was conducted with larger size artificial network simulations and peel tests. The proposed method in this work carries the dual advantages of characterizing actual bonds in a non-woven and characterizing hundreds of bonds simultaneously. The method can be applied to a variety of non-woven fabrics that are bonded at fiber-fiber intersections.

Introduction

Non-wovens are a material class that encompasses all fabrics not manufactured through a weaving or knitting process. A typical non-woven consists of a set of fibers consolidated by either bonding or local entanglement. The manufacturing methods for non-woven are versatile, and the product carries advantages including high porosity, high surface area, and high specific toughness. Because of these positive attributes, non-wovens are utilized in a variety of fields including energy, water purification, ballistic protection, tissue engineering and medical disposables [1–4]. Despite wide application, predicting non-woven strength and toughness remains a difficult task. The deformation process involves many micromechanical mechanisms, such as fiber stretching, fiber bending, fiber rotation and bond damage [5–7]. Among these, bond damage is a major damage mechanism in many non-wovens [5, 8, 9], however, bond strength is rarely reported due to lack of an effective characterization technique. Therefore, the main objective of this work is to develop a method to determine bond strength.

For non-wovens that are bonded at fiber-fiber intersections, randomly distributed bonds connect and transmit loads between individual intersecting fibers. In the seminal work of Cox [10], elasticity for this type of non-woven was derived based on fiber orientation and density, but was not considered to be affected by bonds. However, later finite element simulations showed that Cox's model neither captured local fiber loading mechanisms nor provided satisfactory predictions of macroscopic behavior [11, 12] (especially on sparse networks). It was later found that

✉ M. N. Silberstein
  ms2682@cornell.edu

1 Sibley School of Mechanical and Aerospace Engineering, Cornell University, Ithaca, NY 14850, USA

SEM

bond density indeed affected non-woven elastic modulus. As bond density increases, fiber segment length decreases and fibers tend to deform axially rather than bending [13]. Not only bond density but also bond properties affect non-woven mechanical behavior. Bond damage was found to be the main damage mechanism in paper and geosynthetic materials [5, 8, 9]. By tuning thermal treatment time, temperature, and fiber contact force, non-wovens with different bond properties can be made. The mechanical strength of non-wovens was found to increase with increasing bond strength [14, 15]. Though the importance of bonds has been recognized, accurate bond constitutive behavior has not been used in fiber network modeling. In discrete network simulations where bonds were damageable, bonds were considered as rigid and broke in a brittle manner [11, 12]. Constitutive models incorporated bond damage by introducing a damage variable, but this damage did not have direct relationship to bond properties due to a lack of known bond properties [16, 17].

Precise characterization of bond properties is difficult, since non-wovens are composed of fibers that have diameters on the order of microns or less. Direct testing of bond mechanical behaviors has previously been performed with specially designed tensile testing apparatus or atomic force microscopes (AFM) [18–21]. In these kinds of tests, individual fiber-fiber bonds were made independently rather than extracted from a non-woven. Whether the result reflects bond properties within actual non-wovens needs further proof. Further, it has been found that bond strength within paper has great variance [19, 20], this is likely true for other non-wovens as well. Testing individual bonds one at a time is laborious. When only an estimate of average bonding energy is needed, peel tests can be used [22, 23]. This method provides Mode-I interlayer bonding energy in layered non-woven materials, but does not provide individual bond strength. Processing simulations on fiber pairs have been used to establish the relationship between bond formation conditions (temperature, pressure and fiber lay out) and bond properties. For example, the effect of fiber-fiber angle and degree of indentation on maximum stress in the bonding region was studied using 3D finite element simulations [24]. The work of adhesion between two 'coalesed' polymeric fibers was calculated through atomic simulations [25]. However, these model-prediction results have not been experimentally validated.

Here, we present a new method for characterizing fiber-fiber bond strength in non-wovens. The method is inspired by the advancement of image-based direct modeling. The method carries the dual advantages of characterizing actual bonds in a non-woven and characterizing hundreds of bonds simultaneously. The proposed method is introduced in three steps. In "Bond Strength Determination Procedure", the overall scheme of the method is introduced. In "Materials and Methods" and "Results", the application of the method to a polypropylene non-woven is described. We used a linear irreversible interface law to describe debonding behavior and the model parameters were determined through an optimization process. This interface law has four parameters: normal stiffness k, shear stiffness βk, separation at the start of damage d_1, and separation at total loss of bond stiffness d_2. In "Bond Model Validation", we present two independent validations of the obtained bond strengths.

Bond Strength Determination Procedure

The bond strength determination method proposed in this paper has three ingredients: imaging non-woven microstructure, characterizing mechanical properties, and direct simulation of the force response of specimen microstructure to deformation. The overall procedure is shown in Fig 1. The first step is to image a small specimen with a 3D imaging technique such as micro computed tomography (μCT) or confocal microscopy. This 3D imaging is required to determine fiber arrangement and resolve bonding sites. The size of the specimen should be sufficiently large for the contained bonds to be a representative subset of bonds in a bulk material (> 100 bonds), and sufficiently small to manage imaging and computational cost. After the imaging step, the stress-strain response of this specimen and its constituent fibers are characterized under uniaxial tension. Next, a digital replica of this specimen is extracted from the 3D image. The replica is then discretized and imported into a finite element framework, in which fibers and bonds are explicitly modeled. The fiber stress-strain constitutive behavior is taken directly from single fiber experimental results. Structural elements should be used to model the fibers so that computational efficiency can be improved. A constitutive law has to be chosen to model bond behavior under deformation. The unknown parameters in the constitutive law are estimated through fitting the FEA simulated uniaxial tensile test to the experimental stress-strain results for that specimen. After the model parameters are estimated, bond mechanical properties, like stiffness and strength, can be determined accordingly.

The meso-scale specimen avoids the drawbacks of both component level analysis and continuum level analysis. Local bonding conditions and bond properties usually have great variance, which means getting statistical information of bond properties through individual bond testing is cumbersome. Conversely, within a homogenized framework, resolving bond damage from other irreversible mechanisms, like fiber plasticity and fiber fracture, is challenging. The potential application of this proposed method is broad. It can be applied to any fiber network that is bonded at fiber-fiber intersections (e.g. geosynthetics, paper, electrospun
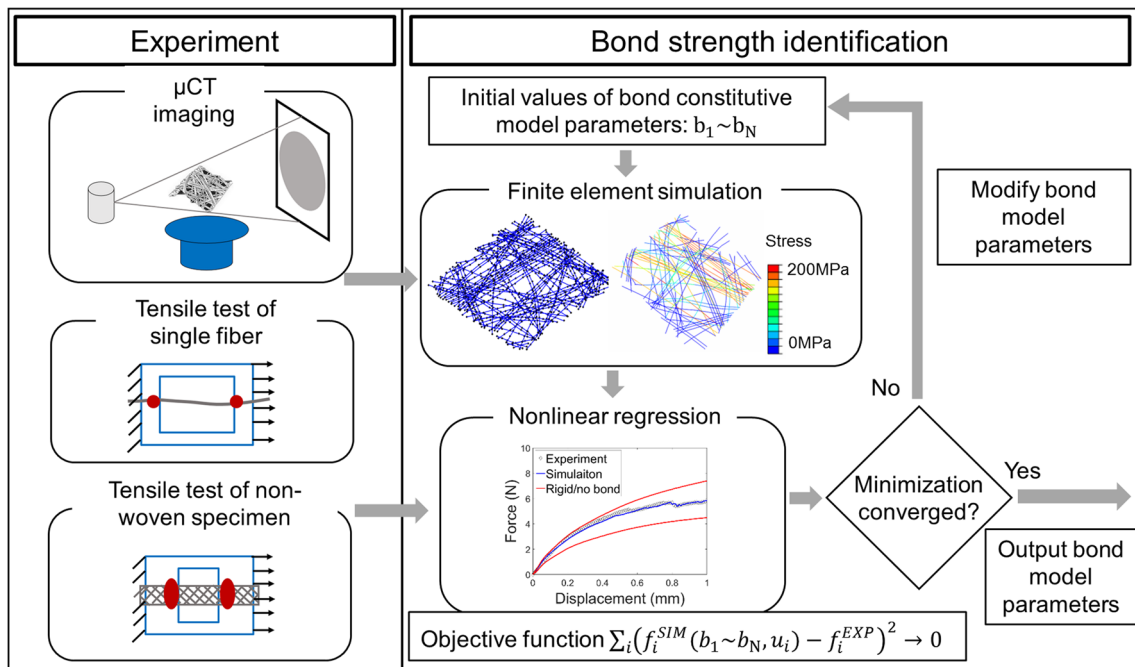
Fig. 1 Procedure for proposed bond strength determination method
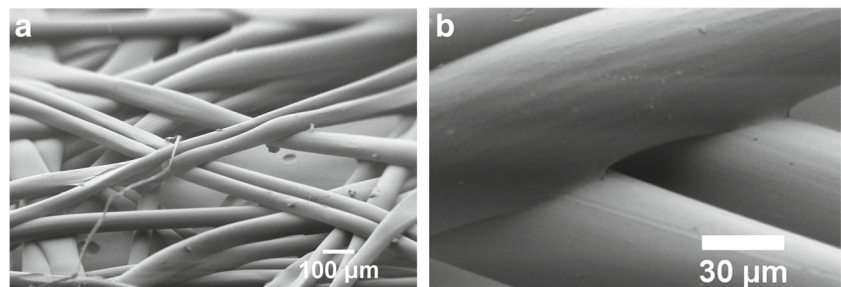
mats) for which damage under macroscopic deformation is a concern.

Materials and Methods

Materials

The method introduced in the previous section is demonstrated here for the Dupont Typar geotextile SF20. This non-woven is composed of polypropylene fibers 40 μm-60 μm in diameter. During the manufacturing process fibers are first laid down on a flat surface and then bonded through application of both heat and mechanical pressure. SEM (scanning electron microscope) images of this material are shown in Fig. 2. Fibers are deformed and partially fused at each bonding site.

The mechanical properties of the Typar SF series of non-woven have previously been characterized in detail [5, 9]. For convenience, the uniaxial tensile and cyclic behavior of SF20 and the constituent fiber are included as Fig. 3. Also, some key observations from the literature are summarized in the following:

– Tensile stress-strain curve of this non-woven presents an elastic region, a roll over yield region and a highly damaged softening region (long tail) after the peak load. The mechanical properties are summarized in Table 1 [9].
– Non-woven mechanical behavior has significant specimen to specimen variation [5, 9].
– The constituent fiber is elastic-visco-plastic. Under tension, the fiber has a short elastic region that transitions into a plastic hardening regime. The mechanical properties are summarized in Table 1 [9].

Fig. 2 SEM images of the non-woven SF20 showing (**a**) the network morphology, (**b**) an enlarged view of the bonding region located in the center of (**a**)

Fig. 3 **a** Uniaxial tensile behavior of non-woven SF20, **b** uniaxial tensile behavior of constituent fiber. "Reprinted from [9], Copyright (2016), with permission from Elsevier"
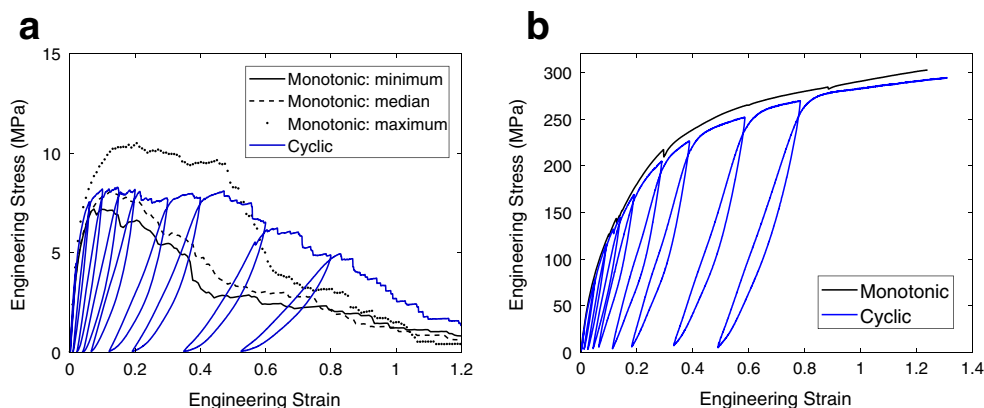
- In cyclic testing, the non-woven modulus at the beginning of each unloading step decreases with deformation, while fiber modulus remains the same. Both fiber fracture and bond fracture contribute to this modulus decrease [9].
- Bond damage in the non-woven is observed starting at small strains (2.5% nominal strain) [5, 9].

Methods

Following the general procedure described in "Bond Strength Determination Procedure", a 2 mm wide non-woven SF20 strip was cut from a bulk sheet and glued (Loctite Plastics Bonding System) to a sample holder spanning across a 2 mm gage length. Within the gage section, there were approximately 500 bonds. The specimens were imaged with a commercial CT (Xradia/Zeiss XRM-520 Versa) with voxel side length set to 3.6 μm. The specimen was then tested under uniaxial tensile loading while the load displacement curve was recorded. The crosshead speed was set to 0.1 mm/min. All specimens were examined before and after testing under an optical microscope (Olympus BH-2) and results from any specimens that showed evidence of fiber slippage from the grip region were discarded.

The μCT 3D image of each specimen was converted into an FEA representation. The microstructure was skeletonized using software FNXCT [26]. This software connects several seed points (manually provided) of one fiber with a third order polynomial curve to represent the centerline of this fiber. After the centerlines of each fiber were determined, a bonding site was introduced at a fiber-fiber intersection if the minimum distance between the two fibers was smaller

than the sum of their radii. The bond area A was calculated using the non-adhesive elastic contact solution [27]

$$A = \pi \sqrt{R_1 R_2} d \tag{1}$$

where R_1, R_2 are fiber radii and $d = (R_1 + R_2 - fiber\ spacing)$ is the indentation distance. The skeletonized fiber network was further discretized into 1D structural elements and then imported into the FE software Abaqus (Fig. 4(a)). The Timoshenko shear flexible beam element (B31) was chosen to mesh fibers due to a relatively short fiber length to diameter ratio (≈ 5). Bonds were modeled by a connector element (CONN3D2), which constitutively defines the interaction between two bonding nodes. Abaqus explicit was used to solve the load-displacement response of the model. All FE simulations were conducted on a desktop with a quad core i7 processor.

Fiber diameters were determined iteratively through image processing and network simulation. An image thresholding step was first applied on the greyscale μCT image to convert it to a binary image. Diameter of a fiber was then measured as the distance from the fiber centerline to the background. All the diameters were measured automatically with image threshold value as the only input. The image threshold value was chosen so that the simulation elastic modulus matches that from the corresponding experiment. Bond locations and areas were updated following adjustment of the image threshold.

We used Ortiz's interfacial cohesive law [28] to describe bond behavior. This law was chosen because of its generality for describing irreversible interface bonding behavior. Bond properties of a cellulose fiber network determined by AFM have also been shown to fit this law [21]. The constitutive equation utilizes four parameters: k, β, d_1 and d_2.

Table 1 Mechanical properties of constituent fibers and nonwoven under uniaxial tensile loading

Material	Young's modulus (GPa)	Tensile strength (MPa)	Failure strain
Fiber	2.45 ± 0.15	293 ± 8	1.3 ± 0.3
Non-woven	0.22 ± 0.02	8.8 ± 1.4	0.15 ± 0.06

Fig. 4 **a** Representative finite element mesh of a specimen. Beam elements are marked as blue lines, bond elements are marked as red lines, nodes are marked as black asterisks. **b** Constitutive behavior of a bond deforming under pure tension. Line with double arrows indicates unloading/reloading path for this bond model
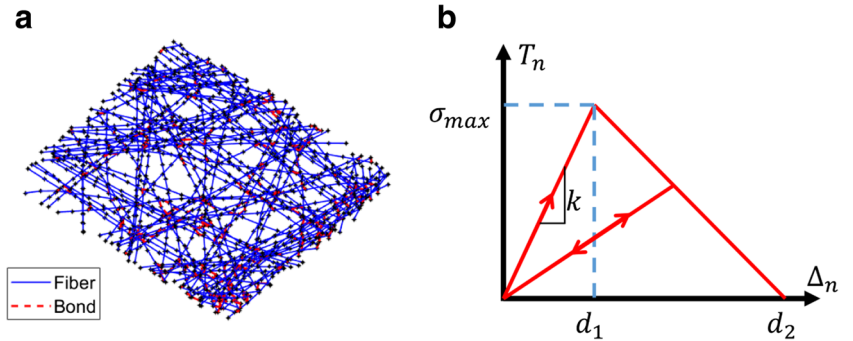
k is bond elastic modulus in normal direction. β describes the relative stiffness of shear deformation to normal deformation. d_1 is the critical distance when damage initiates. d_2 is the critical distance when full separation occurs. Interfacial effective displacement is defined as $\Delta_{eff} = \sqrt{\Delta_n^2 + (\beta \Delta_s)^2}$, where Δ_n is normal displacement and Δ_s is shear displacement [29]. Bond behavior is linear elastic when $\Delta_{eff} \leqslant d_1$, and bond elastic modulus linearly degrades when $d_1 \leqslant \Delta_{eff} \leqslant d_2$. The load displacement response of a bond under normal separation is shown in Fig. 4(b). Bond strengths in pure normal and pure shear deformation mode are calculated as $\sigma_{normal} = k \times d_1$ and $\sigma_{shear} = \beta \times k \times d_1$, respectively.

The parameters in the bond model were determined by fitting the FE simulated uniaxial tensile response to experimental data. The nonlinear regression problem was solved in the least-square sense where the L^2 norm of the residual is minimized. Here, residual $\boldsymbol{r}$ describes the difference between simulated force response $\boldsymbol{f}^{sim}$ and experimental force response $\boldsymbol{f}^{exp}$ at each data point:

$$\boldsymbol{r}(\boldsymbol{b}) = \{\boldsymbol{f}^{sim}(\boldsymbol{b}) - \boldsymbol{f}^{exp}\} \in \mathbb{R}^{N_D}, \tag{2}$$

where $\boldsymbol{b}$ is a vector of bond parameters $\{k, \beta, d_1, d_2\}$ and N_D is the number of data points. The regression problem is stated (considering the positiveness of bond parameters) as:

$$\text{minimize} \quad g(\boldsymbol{b}) = \frac{1}{2}\|\boldsymbol{r}(\boldsymbol{b})\|_{L_2} = \frac{1}{2}\boldsymbol{r}^T(\boldsymbol{b})\boldsymbol{r}(\boldsymbol{b}) \tag{3}$$

$$\text{subject to} \quad b_i > 0 \tag{4}$$

The objective function $g(\boldsymbol{b})$ is non-smooth due to bond damage along the deformation process. A downhill simplex algorithm [30] was used to solve the optimization problem, since a gradient based optimization algorithm would suffer from convergence issues. A simplex is a polytope with $N+1$ vertices in an N dimensional optimization problem. The downhill simplex algorithm starts with constructing a simplex around the initial guess and then takes a series of steps to change simplex shape and move it along the N dimensional topography until it reaches a minima. The direction of simplex shape change depends solely on function evaluations at each vertex. In the present study the downhill simplex method converged in around 15 steps.

Results

Network Microstructure Statistics

The microstructure statistics corresponding to six specimens are listed in Table 2. Due to the small specimen size the specimen microstructure (arrangement of fibers and bonds) varies significantly. Fiber number ranges from 90 to 138 and total fiber length ranges from 170 mm to 281 mm. These ranges are self-consistent since fibers are long and should span across the 2 mm specimen region in this non-woven. The number of bonds ranges from 305 to 1026. In plane fiber orientation distribution can be described by an orientation parameter p [9], which is defined as: $p = 2\langle \cos^2 \alpha \rangle - 1$,

Table 2 Microstructure statistics and mechanical properties of six tested non-woven specimens

	Number of fibers	Total fiber length [mm]	Number of bonds	Orientation parameter	Stiffness [N/mm]	Peak load [N]
Specimen 1	106	206	566	−0.055	21.6	8.7
Specimen 2	97	180	629	0.23	23.4	7.0
Specimen 3	138	281	503	0.14	19.4	9.6
Specimen 4	90	170	338	−0.14	16.5	5.9
Specimen 5	130	242	1026	−0.19	22.6	6.1
Specimen 6	107	206	305	0.23	22.7	8.9
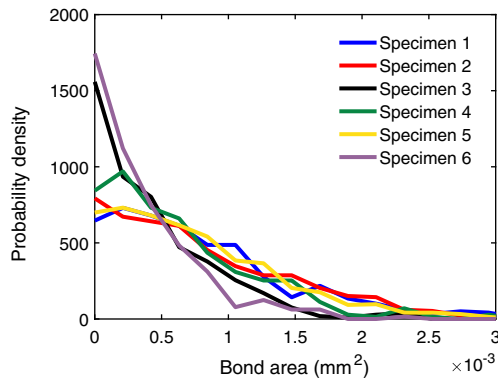
Fig. 5 Bond area distribution within tested specimens

where α is the angle between the fiber axis and the direction of applied strain. This parameter varies from -1 to 1 and equals 0 for a set of fibers randomly oriented in plane. The orientation parameter of the six specimens ranges from -0.19 to 0.23, indicating a nearly uniform fiber orientation distribution. The bond area distribution is shown in Fig. 5, this distribution is skewed towards small bonding area. The variation in bond area distribution, fiber segment number, and fiber orientation distribution indicates that each specimen has a unique fiber layout and therefore load transmission path. Consequently, the bond strength identification

is evaluated by consistency of the bond model parameters estimated from these six different specimens.

Model Parameter Study

The bond model has four parameters: k, β, d_1, d_2. The value ranges of the four parameters that define the bond constitutive behavior can be estimated based on the physical meaning of each. Since bonds are formed from two fibers, the bond elastic stiffness k should be of the same order as the fibers. If the bond elastic modulus has the same value as its constituent fibers then $k = E_f / l_{ch}$. Since the fiber modulus is $E_f = 2.4$ GPa, and the characteristic length scale l_{ch} is the average fiber-fiber distance at a bonding site, $l_{ch} \approx 30$ μm, $k = 80$ MPa/μm. β controls the relative stiffness between shear deformation and normal deformation. Based on the suggestions in [29], β is typically below 1. Here, we take $\beta = 0.7$ as a reference for the parameter study. d_1 and d_2 describe the displacement between ends of the bond connector element and therefore should be on the scale of microns.

Comparing with the reference case ($k = 80$ MPa/μm, $\beta = 0.7$, $d_1 = 3\mu$m, $d_2 = 3\mu$m), each of the four parameters was modified by a factor of two to see its effects on macroscopic behavior and damage progression (Fig. 6). Prior to damage, the simulated curves fall on the rigid bond

Fig. 6 **a** Load displacement curves for parameter study of k and d_1, and **b** corresponding damage progression curves. **c** Load displacement curves for parameter study of β and d_2, and **d** corresponding damage progression curves
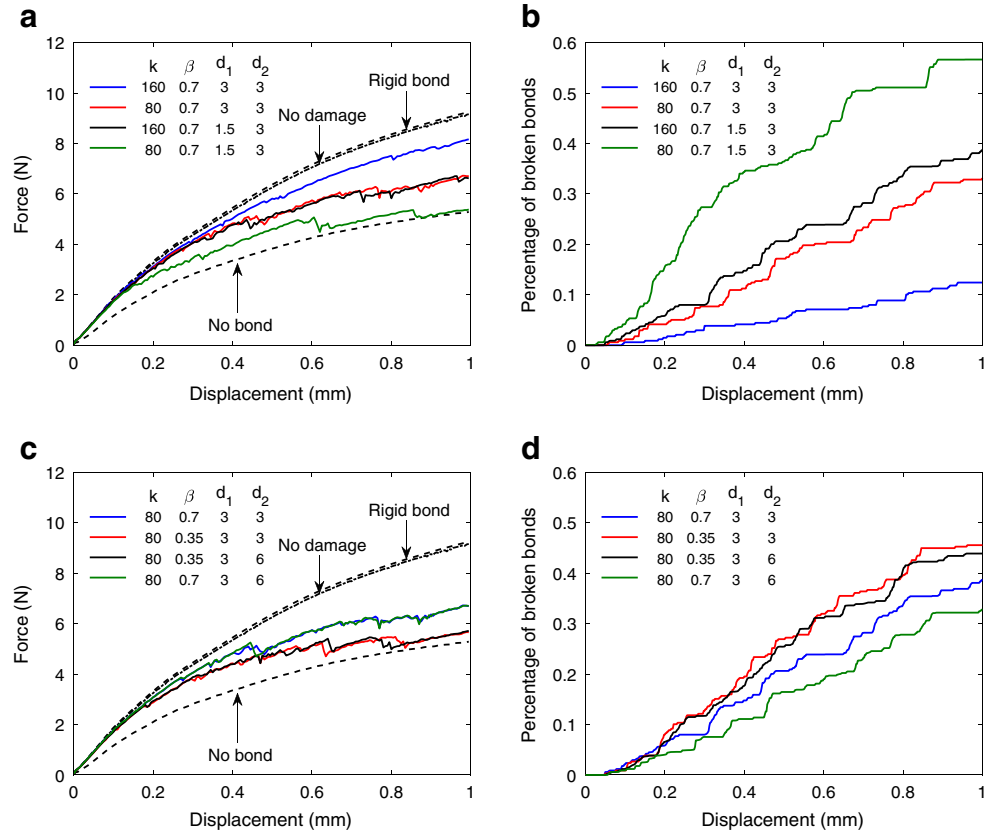
line for both $k = 80$ MPa/μm and $k = 160$ MPa/μm cases indicating that network elastic stiffness is minimally influenced by bond stiffness. This lack of dependence on bond stiffness has also been observed in literature [12]. When bond damage is considered, parameters d_1 and d_2 come into play. Bond strength σ_{normal} and σ_{shear} are both proportional to $k \times d_1$. For high k or d_1 cases, bonds are stronger, fewer bonds are broken during the tests, and more fibers participate in load carrying (Fig. 6(a)–(b)). Systematic variations in k or d_1 reveal that the model is sensitive to σ_{normal} rather than k and d_1 independently. The effects of β and d_2 are shown in Fig. 6(c)–(d). Similarly to σ_{normal}, higher β results in higher force response and less bond damage inside the network. However, the effect of β is less significant than σ_{normal} when they are changed by same percent. The model response is not sensitive to d_2, so in later sections d_2 is set equal to d_1.

Bond Strength Estimation

The load displacement curves of six tested specimens are shown in Fig. 7. All the curves have a linear region, a smooth roll-over region and then a kinked region starting at displacement ≈ 0.4 mm. These kinks come from bond frac-ture and associated fiber stress relaxation. Occasionally, a large number of bonds broke within a short period of time and caused a big force drop. Comparing Figs. 3(a) and 7, it should be noted that the load displacement curve of the 2 mm $\times$ 2 mm specimens are jagged compared to larger specimens. This indicates that damage in larger size specimens is distributed while damage in small specimens is more localized and apparent even before the peak load. These smaller specimens are therefore better for extracting bond parameters. The six tested specimens have distinct microstructures and correspondingly their load-displacement curves vary significantly from each other. Specimens 1, 2, 5 and 6 have similar elastic moduli even though their total fiber lengths ($\propto$ areal weight) are different. Specimen 3 has higher total fiber length but its elastic modulus is lower. Specimen 4 has the lowest fiber length and elastic modulus. From this data it is apparent that different network microstructures have different load transmission paths and different bond breaking sequences. A discrete network model that captures the specific network microstructure has the advantage of simulating real damage progression within different specimens.

For each specimen, we solved a nonlinear least square problem (equations (3) to (4)) to obtain bond parameters β and d_1. The bond model estimation results are shown in
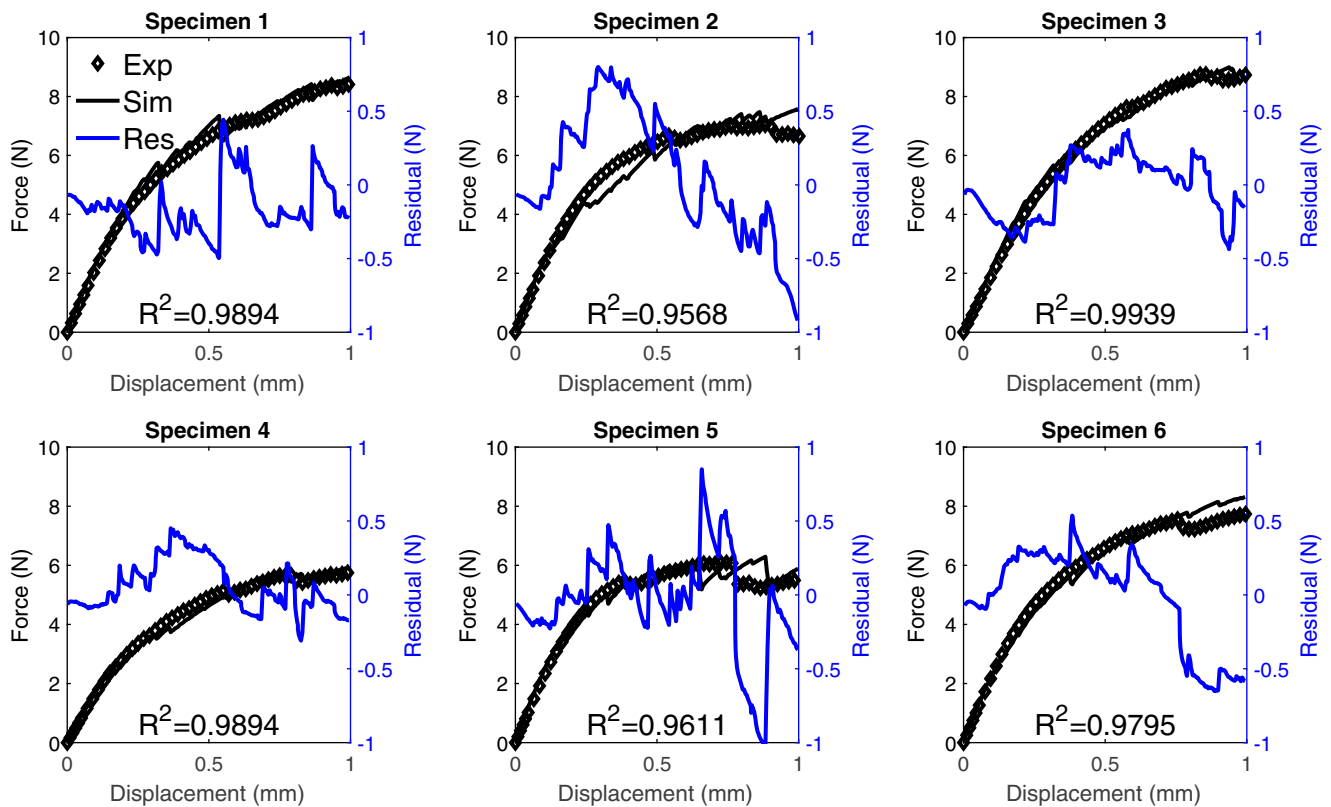
Fig. 7 Uniaxial tensile response (diamond markers) of six tested non-woven specimens. FE simulation results (solid black line) with estimated bond model are overlaid on the experimental curves. The residual (solid blue line) and goodness of fit (R^2 value) are also reported in each subplot

Table 3 Mean bond strength for each non-woven specimen and goodness of fit for individual optimization and cross-validation

	Normal strength σ_{normal} [MPa]	Shear strength σ_{shear} [MPa]	Individual fit R^2	Cross validation R^2
Specimen 1	170	133	0.9894	0.8832
Specimen 2	89	72	0.9568	0.8550
Specimen 3	147	98	0.9939	0.9909
Specimen 4	133	97	0.9894	0.9548
Specimen 5	116	72	0.9611	0.8084
Specimen 6	140	112	0.9795	0.9639

Fig. 7 and Table 3. Individual fitting results show that the model captures the roll-over yield region and major kinks on the load displacement curve. Residual *r* versus displacement is overlaid on Fig. 7 as well. In specimens 1, 3, 4 and 6, the residual is small indicating a good fit. In the other specimens, the residual is continuously positive in one region and negative in another. This indicates that model overestimates bond strength in one region and underestimates it in another. One possible reason for this error is the assumption we made that bond strength is proportional to bond area however, the bonding nature may be more complicated. While a more complex bond model could be used, a strong physical basis would be needed to avoid over fitting. Table 3 lists estimated bond normal strength and shear strength. Calculating the mean and standard deviation of bond strengths in the six specimens, we have $\sigma_{normal} = (1.3 \pm 0.3) \times 10^2$ MPa, and $\sigma_{shear} = (1.0 \pm 0.2) \times 10^2$ MPa. Specimens 2 and 5 have poorer fit and much lower bond strength than the other specimens. Both of these specimens have less hardening at finite strains. While this reduced hardening is most likely a reflection of low bond strength, it could also have a contribution from small slipping of the fibers at the grip that was not evident within optical microscopy.

Cross validation evaluates how fitted model parameters can be generalized to a new data set. In this work, each of the six tested specimens represents an independent data set due to its unique network microstructure. We performed leave-one-out cross validation on each individual data set, using five data sets for training to get model parameters and then testing the fidelity of obtained model parameters on the left out data set. This process was repeated until all data sets had been left out once. Table 3 shows the cross validation results. Full fit and residual plots are provided in Appendix A. All validation simulations have reasonably good agreement with experimental data, showing the predictive power of the obtained bond model parameters. Not surprisingly, specimens 2 and 5 have the worst fits since their independent fitted bond strengths are lower than the other specimens.

Bond Model Validation

Larger Size Specimen Validation

Macroscopic damage in non-wovens can be quantitatively characterized by cyclic tests. The slope at the beginning of each unloading step decreases with deformation due to a loss of network connectivity caused by bond fracture [5, 9]. This observation provides a way to test the validity of bond strength values obtained in the previous section. We performed cyclic tests on 6 mm × 6 mm non-woven specimens and FE simulations of the same size artificial random fiber network (RFN). The size of 6 mm × 6 mm is chosen because at this larger size the response is reasonably insensitive to the specific microstructure and the FE simulation can be done in a timely manner on a typical desktop. The method and result of the validation approach are discussed in this section.

Methods In the cyclic experiment, a non-woven specimen was stretched to a certain strain and then unloaded to zero force and reloaded again. The displacements at the start of each unloading step were 0.12 mm, 0.36 mm, 0.6 mm, 0.9 mm, 1.2 mm, 1.8 mm, 2.4 mm, 3.6 mm, 4.8 mm, and both load and unload speeds were set to 0.0353 mm/s. A total of five specimens were tested. The computational work started by an RFN generation step. The generation algorithm first generated random seeds within the specimen domain (6 mm × 6 mm × 0.3 mm). A straight fiber was then extended from each seed point to the boundaries of the domain. The fiber was assumed to have uniform in-plane angle (randomly drawn from a uniform distribution of 0° to 180°), and a slight out of plane angle (randomly drawn from a normal distribution of 0° to 3°). Fiber diameter and network density were set to the same as measured by μCT and the network generation step was stopped when the network density reached target value (43 mm/mm^2 from Table 2). After all fibers were generated, bonding sites were located and bond areas were calculated following the same procedure as described in "Methods". Since the fiber generation step did not prevent fibers from passing through each other,
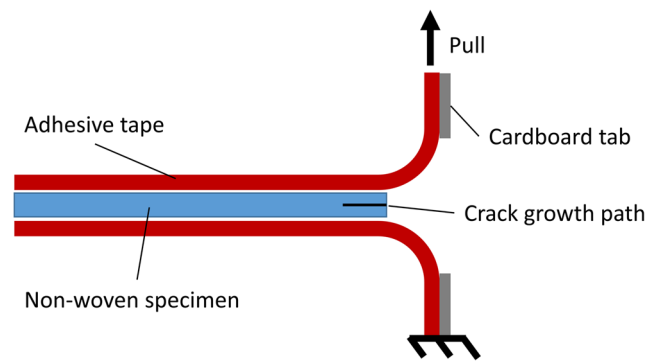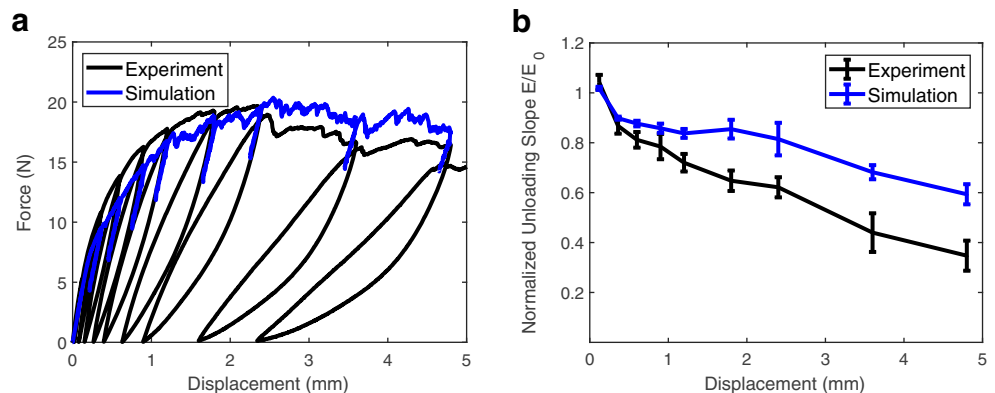
bond area distribution in the RFN is different from the real material (Fig 5). The nodes at each bonding sites were tweaked along the bond vector so that bond area distribution matches experimental data. The generated RFN was further discretized and imported into the finite element framework and simulated with unloading at the same displacements as the cyclic experiment.

Result One representative cyclic test result is shown in Fig. 8(a). The specimen reaches peak load at a displacement of 2 mm and then the force decreases. We measured unloading slopes at the beginning of each unloading step (Fig. 8(b)). The unloading slope slightly increases at small strains possibly due to fiber alignment and then the unloading modulus drops because of bond damage. One representative simulation load-displacement curve is overlaid on Fig. 8(a). The simulation result captures the reload to the stress at which unloading started. In the simulation no damage was observed during unloading, so the duration of the unloading step is not important. Since the artificial network is not a replica of specimen geometry, the exact force response is different from the experiment. Fig. 8(b) shows that the simulation unloading slope reduction with increasing displacement has good agreement with experiment, thereby validating the utility of the bond model results in predicting damage progression. The mismatch at finite strains comes from either geometry simplification of RFN or potential fiber fracture in experiment. We found that increasing fiber out-of-plane angles would give a better match of damage progressions. But in this case, many fiber ends were on RFN surfaces instead of edges which was not observed in a real non-woven specimen. So the current out-of-plane angle distribution was adopted. It should be noted that no fitting parameters are included in these artificial network simulations.

Peel Tests

Peel testing provides a way to experimentally characterize average non-woven bonding energy. As shown in Fig. 4(a)


Fig. 9 Schematic of the specimen used for peel tests. Two adhesive tapes were attached on a non-woven specimen and the tail of each adhesive tape was attached to a cardboard tab for clamping. The crack grew in the middle of the non-woven specimen during peeling, leading to separation of layers

and Chen. et. al. [9], fibers in the non-woven SF20 are overlaid on each other forming a multi-layered structure. The ply adhesion energy can be estimated as the total work needed to break all the bonds between the two adjacent layers. The number of bonds within one layer can be obtained from μCT images. Therefore, energy dissipation per bond broken can be approximated by dividing the ply adhesion energy by the number of bonds between two adjacent layers. A similar approach has been applied for paper [22, 23]. Assuming normal separation, the expected energy dissipation per bond can be estimated from the obtained bond model parameters(Appendix A). We used this method to verify the bond strength values obtained with our image based modeling method.

A T-shaped specimen was adopted for the peel test (Fig 9). The specimen was made by putting two pieces of adhesive tape on opposite sides of a 20 mm × 100 mm piece of SF20 to form a sandwich structure. Each adhesive tape extended beyond the non-woven and was attached to a cardboard tab for clamping. In the test, the lower cardboard tab was fixed and the upper tab was pulled at a constant speed

Fig. 8 Bond strength values are tested on large size network simulations under cyclic loading. **a** Load displacement curves of a representative experiment and a representative artificial network simulation for a 6 mm × 6 mm specimen. **b** Unloading slope normalized by initial elastic modulus. The mean and standard deviation of five experimentally tested specimens and random network simulations are shown

of 0.5 mm/s. The peel force reached a peak at the beginning of a test and then oscillated within a small range, indicating static peeling (Fig 10). The non-woven specimen was fractured along a crack plane and separated into two thinner pieces. If the crack propagation direction deviated from initial interface plane, the data of the specimen was discarded. Since both adhesive tape and non-woven are thin (less than 1 mm), the elastic energy of bending was ignored in the data analysis. Most of the external work in the peel test was supplied to separating bonded layers.

A total of five specimens were tested. Three representative load-displacement curves are shown in Fig. 10. The ply adhesion energy of these five specimens is 0.12 ± 0.01 kJ/m^2. Since it is observed in the μCT data that the number of bonds per mm^2 is 120 ± 50 and the number of layers is ≈ 7, the bond number density between two adjacent layers in a T-peel specimen is ≈ 20 per mm^2. The energy dissipation per bond broken is determined by dividing ply energy by total number of bonds between two adjacent layers, and reads $(5.8 \pm 0.3)\mu$J. The energy dissipation per bond broken can also be estimated using the obtained bond strength values from the proposed method (Table 3). When a bond is broken in the peel test, energy is dissipated through the separation of two bonding surfaces and the relaxation of the fibers connected to this bond. Assuming all bonds are broken under mode-I loading, energy dissipation per bond broken is calculated as $(1.8 \pm 0.8)\mu$J (Appendix B). This value has the same order of magnitude as the one obtained in the peel test, validating the proposed method. Bond strength is likely overestimated in the peel tests because we ignored the energy dissipation away from the fiber-fiber interface. It should also be pointed out that since the exact number of broken bonds on the crack face is unknown, peel tests can only provide a rough estimation of average bond energy.
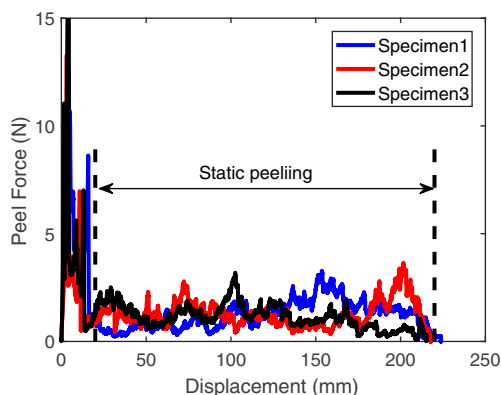
Fig. 10 Peel test force - displacement curves of three representative specimens. The static peeling region used for the bond energy calculation is indicated

Conclusion

In this work, we introduce a new method that uses a combination of experimental work and imaged-based modeling to characterize bond properties in non-woven fabrics. In the experimental portion, a non-woven specimen is imaged and then loaded for mechanical characterization. In the computational portion, the undeformed specimen microstructure is discretized and imported into a finite element framework. Since both fibers and bonds are explicitly represented in the finite element model, bond properties can be determined by solving the inverse problem of matching simulated mechanical response to experimental data. We demonstrate the application of this method to a commercial polypropylene non-woven. A bilinear irreversible interfacial law was used to constitutively prescribe bond behavior, and the parameters in this bond model were estimated for each tested non-woven specimen. A cross validation procedure showed that the estimated model parameters can be applied to new data sets to predict non-woven uniaxial tensile behaviors. Simulations of artificial networks showed that the estimated bond strengths can give accurate predictions of damage progression in larger size non-woven specimens. Single bond energy was also confirmed by peel tests, which provided an average interlayer bonding energy measurement.

The proposed method provides a feasible way to characterize a large number of bonds in non-wovens that are bonded at fiber-fiber intersections. The framework of using image based model to identify component behavior can also be applied to other 3D structural materials as well. The measured bond properties will also serve as good resources for building constitutive models in the future.

Appendix A: Fitted Bond Parameters

The bond parameter estimation results of individual fitting and cross validation are shown in Table 4. The obtained values have good consistency among tested specimens. Figure 11 shows the cross validation results. The finite element simulation captures the overall trend of the experimental load-displacement curve, even though the optimiza-

**Table 4** Optimization results for individual fit and cross-validation

Individual fit			Cross validation		
Specimen number	β	d_1 [μm]	Left-out specimen	β	d_1 [μm]
1	0.782	2.12	1	0.795	1.43
2	0.811	1.11	2	0.593	1.82
3	0.665	1.83	3	0.891	1.34
4	0.734	1.66	4	0.695	1.52
5	0.615	1.46	5	0.656	1.63
6	0.801	1.75	6	0.731	1.48

tion process does not use the experimental data of that specimen. Iterations 2 and 5 have higher simulation force responses than experiments, while the other four iterations show the opposite behavior. This difference is because both specimen 2 and 5 have relatively low bond strength values when fitted independently (Table 3), so they lower the bond strength estimations in the cross validation step when one iteration takes them as part of the training set. As mentioned in the earlier text, specimen 2 and 5 are suspectable of fiber slippage and hence underestimating bond strength values. This may be the reason for the mismatch

of simulation and experimental load-displacement curve in this cross validation step.

Appendix B: Peel Test Analysis

Figure 12 shows a simplified loading scenario at the crack tip in a peel test. One bond is connected to four fiber segments and each fiber segment is connected to the rest of non-woven network structure. When a bond is taking up load, two fiber segments are under tension. When a bond is
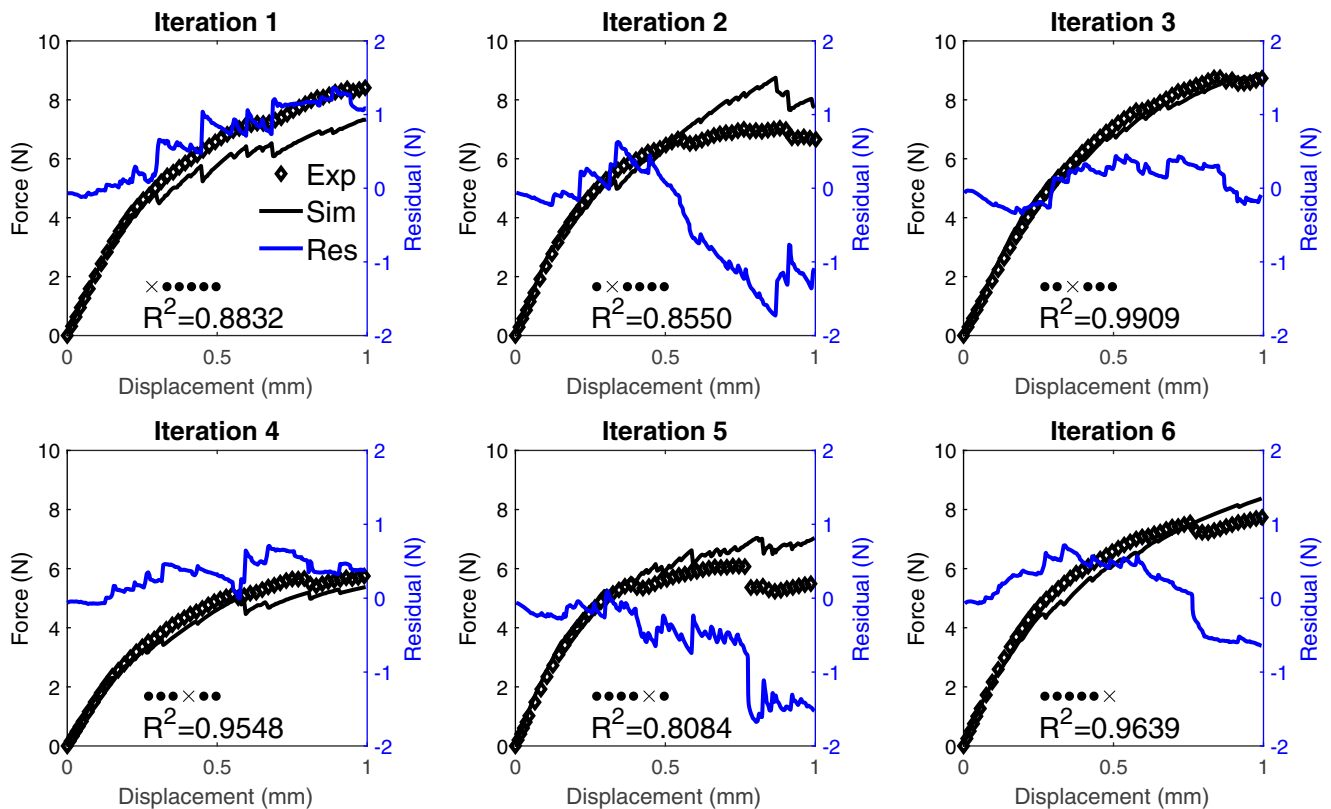
Fig. 11 Leave-one-out cross validation results. Bond model parameters obtained from training data sets are tested on the left out test data set. The schematic label shows the partition of each iteration, where "×" represents the test data set and "•" represents the training data set. The simulated load-displacement curve, residual and R^2 value of each iteration are shown
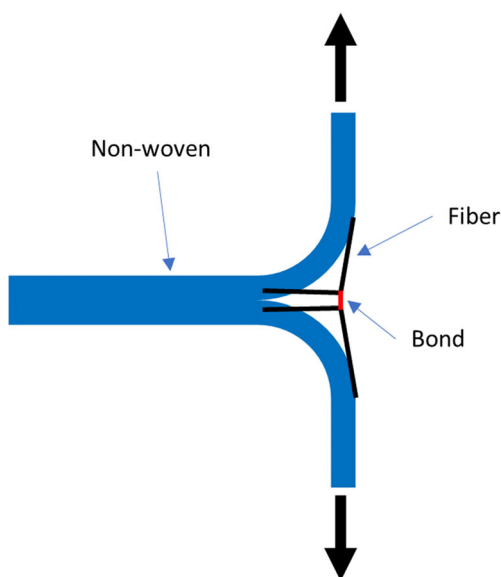
Fig. 12 The loading approximation of the crack tip in peel tests

broken, the total energy dissipation (U_{total}) comes from the energy to separate bonded interfaces (U_b) and the relaxation of strain energy in fibers connected to this bond (U_f).

$$U_{total} = U_b + U_f \quad (5)$$

Assuming normal bond separation, U_b can be calculated using the cohesive zone model parameters (Table 4):

$$U_b = \frac{1}{2} \times \sigma_{normal} \times A \times d_1 = (0.10 \pm 0.03)\mu J \quad (6)$$

where A is the bond area.

U_f is the strain energy stored in the two stretched fibers and can be calculated as:

$$U_f = \frac{(\sigma_{normal} \times A)^2 \times L_{seg}}{E \times \pi R^2} = (1.7 \pm 0.8)\mu J \quad (7)$$

where $L_{seg} = 0.2$mm is the fiber segment length, $E = 2400$MPa is the fiber modulus and $R = 20\mu$m is the fiber radius.

Summing up equations (6) and (7), we have

$$U_{total} = (1.8 \pm 0.8)\mu J \quad (8)$$

as the predicted energy per bond fracture during the static peel test regime.

References

1. Liu DS, Ashcraft JN, Mannarino MM, Silberstein MN, Argun AA, Rutledge GC, Boyce MC, Hammond PT (2013) Spray layer-by-layer electrospun composite proton exchange membranes. Adv Funct Mater 23(24):3087–3095
2. Russell SJ (2006) Handbook of nonwovens. Woodhead Publishing, Sawston
3. Yoon K, Hsiao BS, Chu B (2008) Functional nanofibers for environmental applications. J Mater Chem 18(44):5326–5334
4. Ahmed FE, Lalia BS, Hashaikeh R (2015) A review on electro-spinning for membrane fabrication: challenges and applications. Desalination 356:15–30
5. Ridruejo A, González C, LLorca J (2011) Micromechanisms of deformation and fracture of polypropylene nonwoven fabrics. Int J Solids Struct 48(1):153–162
6. Silberstein MN, Pai CL, Rutledge GC, Boyce MC (2012) Elastic–plastic behavior of non-woven fibrous mats. J Mech Phys Solids 60(2):295–318
7. Chen Y, Ridruejo A, González C, Llorca J, Siegmund T (2016) Notch effect in failure of fiberglass non-woven materials. Int J Solids Struct 96:254–264
8. Isaksson P, Gradin P, Kulachenko A (2006) The onset and progression of damage in isotropic paper sheets. Int J Solids Struct 43(3):713–726
9. Chen N, Koker MK, Uzun S, Silberstein MN (2016) *In-situ* x-ray study of the deformation mechanisms of non-woven polypropylene. Int J Solids Struct 97:200–208
10. Cox H (1952) The elasticity and strength of paper and other fibrous materials. British Journal of Spplied Physics 3(3):72
11. Åström J, Saarinen S, Niskanen K, Kurkijärvi J (1994) Microscopic mechanics of fiber networks. J Appl Phys 75(5):2383–2392. https://doi.org/10.1063/1.356259
12. Räisänen V, Alava M, Niskanen K, Nieminen R (1997) Does the shear-lag model apply to random fiber networks? J Mater Res 12(10):2725–2732
13. Shahsavari A, Picu R (2013) Elasticity of sparsely cross-linked random fibre networks. Philos Mag Lett 93(6):356–361
14. Torgnysdotter A, Kulachenko A, Gradin P (2007) The link between the fiber contact zone and the physical properties of paper: a way to control paper properties. J Compos Mater 41(13):1619–1633
15. Choi SS, Lee SG, Joo CW, Im SS, Kim SH (2004) Formation of interfiber bonding in electrospun poly (etherimide) nanofiber web. J Mater Sci 39(4):1511–1513
16. Ridruejo A, González C, LLorca J (2012) A constitutive model for the in-plane mechanical behavior of nonwoven fabrics. Int J Solids Struct 49(17):2215–2229
17. Isaksson P, Hägglund R, Gradin P (2004) Continuum damage mechanics applied to paper. Int J Solids Struct 41(16):4731–4755
18. Torgnysdotter A, Kulachenko A, Gradin P (2007) Fiber/fiber crosses: finite element modeling and comparison with experiment. J Compos Mater 41(13):1603–1618
19. Schmied FJ, Teichert C, Kappel L, Hirn U, Schennach R (2012) Joint strength measurements of individual fiber-fiber bonds: an atomic force microscopy based method. Rev Sci Instrum 83(7):073,902
20. Schmied FJ, Teichert C, Kappel L, Hirn U, Bauer W, Schennach R (2013) What holds paper together: Nanometre scale exploration of bonding between paper fibres. Sci Rep 3:2432
21. Kulachenko A, Uesaka T (2012) Direct simulations of fiber network deformation and failure. Mech Mater 51:1–14
22. Koubaa A, Koran Z (1995) Measure of the internal bond strength of paper/board. Tappi J 78(3):103–112
23. Yousefi Shivyari N, Tajvidi M, Bousfield DW, Gardner DJ (2016) Production and characterization of laminates of paper and cellulose nanofibrils. ACS Appl Mater Interfaces 8(38):25,520–25,528
24. Berhan L, Sastry A (2003) On modeling bonds in fused, porous networks: 3d simulations of fibrous–particulate joints. J Compos Mater 37(8):715–740
25. Buell S, Rutledge GC, Vliet KJV (2010) Predicting polymer nanofiber interactions via molecular simulations. ACS Appl Mater Interfaces 2(4):1164–1172

26. Wernersson EL, Borodulina S, Kulachenko A, Borgefors G (2014) Characterisations of fibre networks in paper using micro computed tomography images. Nord Pulp Pap Res J 29(3):468–475

27. Popov V (2010) Contact mechanics and friction: physical principles and applications. Springer Science & Business Media, Berlin

28. Ortiz M, Pandolfi A (1999) Finite-deformation irreversible cohesive elements for three-dimensional crack-propagation analysis. Int J Numer Methods Eng 44(1998):1267–1282

29. Bower AF (2009) Applied Mechanics of Solids. CRC press, Boca Raton

30. Nelder JA, Mead R (1965) A simplex method for function minimization. Comput J 7(4):308–313